Resolved Lyman-α properties of a luminous Lyman-break galaxy in a large ionised bubble at $z = 6.53$

Jorryt Matthee[1]⋆, David Sobral[2], Max Gronke[3]†, Gabriele Pezzulli[1],
Sebastiano Cantalupo[1], Huub Röttgering[4], Behnam Darvish[5], Sérgio Santos[2]

[1] *Department of Physiscs, ETH Zürich, Wolfgang-Pauli-Strasse 27, 8093 Zürich, Switzerland*
[2] *Department of Physics, Lancaster University, Lancaster, LA1 4YB, UK*
[3] *Department of Physics and Astronomy, University of California, Santa Barbara, USA*
[4] *Leiden Observatory, Leiden University, PO Box 9513, NL-2300 RA Leiden, The Netherlands*
[5] *Cahill Center for Astrophysics, California Institute of Technology, 1216 East California Boulevard, Pasadena, CA 91125, USA*

11 December 2019

ABSTRACT

The observed properties of the Lyman-α (Lyα) emission line are a powerful probe of neutral gas in and around galaxies. We present spatially resolved Lyα spectroscopy with VLT/MUSE targeting VR7, a UV-luminous galaxy at $z = 6.532$ with moderate Lyα equivalent width (EW$_0 \approx 38$ Å). These data are combined with deep resolved [CII]$_{158\mu m}$ spectroscopy obtained with ALMA and UV imaging from *HST* and we also detect UV continuum with MUSE. Lyα emission is clearly detected with S/N ≈ 40 and FWHM of 374 km s^{-1}. Lyα and [CII] are similarly extended beyond the UV, with effective radius r$_{\rm eff} = 2.1 \pm 0.2$ kpc for a single exponential model or r$_{\rm eff,Ly\alpha,halo} = 3.45^{+1.08}_{-0.87}$ kpc when measured jointly with the UV continuum. The Lyα profile is broader and redshifted with respect to the [CII] line (by 220 km s^{-1}), but there are spatial variations that are qualitatively similar in both lines and coincide with resolved UV components. This suggests that the emission originates from two components with plausibly different HI column densities. We place VR7 in the context of other galaxies at similar and lower redshift. The Lyα halo scale length is similar at different redshifts and velocity shifts with respect to the systemic are typically smaller. Overall, we find little indications of a more neutral vicinity at higher redshift. This means that the local (~ 10 kpc) neutral gas conditions that determine the observed Lyα properties in VR7 resemble the conditions in post-re-ionisation galaxies.

Key words: galaxies: high-redshift – cosmology: observations – galaxies: evolution – cosmology: dark ages, reionisation, first stars

1 INTRODUCTION

The re-ionisation epoch marks the transition of intergalactic hydrogen from neutral to ionised. Such transition is thought to occur between $z \approx 6 - 10$ (Fan et al. 2006; Planck Collaboration et al. 2015; Bañados et al. 2018). However, the exact timing and topology of re-ionisation and the major origin of ionising photons are not well known.

Due to the sensitivity of the Lyman-α (Lyα; $\lambda_0 = 1215.67$ Å) equivalent width (EW) in high-redshift galaxies to neutral hydrogen (e.g. Dijkstra et al. 2007), it has been extensively explored as a probe of the evolving neutral fraction in the epoch of re-ionisation (e.g. Stark et al. 2010;

Pentericci et al. 2014). However, in addition to the EW, more subtle variations in the Lyα line profile and spatial extent are also expected (e.g. Mas-Ribas et al. 2017), but are difficult to explore at $z > 6$ (c.f. Hu et al. 2010; Momose et al. 2014; Kakuma et al. 2019).

One effect of an increasing neutral fraction is a reduced transmission of Lyα photons at increasingly redder wavelengths with respect to the systemic redshift (e.g. Laursen et al. 2011). How this affects the observed Lyα properties depends on the velocity shift between Lyα and the systemic redshift (e.g. Choudhury et al. 2014; Mason et al. 2018), for example due to outflows (e.g. Erb et al. 2014; Rivera-Thorsen et al. 2015).

Currently, velocity shifts between the peak of the Lyα line and the systemic redshift at $z > 6$ are measured with

⋆ Zwicky Fellow – mattheej@phys.ethz.ch
† Hubble Fellow

other rest-frame UV lines (e.g. Stark et al. 2017) or through measurements of far-infrared lines with ALMA (e.g. Pentericci et al. 2016; Hashimoto et al. 2018). The interpretation of *observed* velocity shifts at $z > 6$ is challenging: a large observed shift could be intrinsic if, for example, outflows redshift Lyα photons out of the resonance wavelength (Verhamme et al. 2006) before encountering significant amount of neutral hydrogen so that the intervening intergalactic medium (IGM) is effectively transparent (Dijkstra 2014). A larger observed shift could also be the consequence of a decreased transmission due to large amounts of neutral hydrogen around galaxies which in practice absorbs the bluer part of the line (e.g. Laursen et al. 2011; Smith et al. 2019). Finally, large shifts could also be consequences of large velocity offsets between (blended) merging components, with lines corresponding to different components.

The spatial extent of Lyα emission may increase in the epoch of re-ionisation due to an increased importance of resonant scattering in the presence of more neutral hydrogen in the circum galactic medium (CGM) of galaxies. An indication of an increase in the Lyα scale length is found between $z = 5.7$ and $z = 6.6$ by Momose et al. (2014), but those results rely heavily on stacking (see also Santos et al. 2016). Recently, the Multi Unit Spectroscopic Explorer (MUSE) instrument on the VLT (Bacon et al. 2010) has been successful in observing extended Lyα emission around individual high-redshift galaxies (e.g. Wisotzki et al. 2016; Leclercq et al. 2017), but so far has focused mostly on faint Lyman-α emitters (LAEs) at $z < 6$.

Due to their brightness, luminous Lyα emitters are the best targets to take studies of extended Lyα emission into the epoch of re-ionisation ($z > 6$). Among the sample of luminous LAEs (e.g. Sobral et al. 2018), VR7 is the brightest in the UV continuum ($M_{1500} = -22.4$) and consequently has a relatively typical Lyα equivalent width (EW), $EW_0 = 38$ Å in spite of its luminous Lyα emission. This is similar to the typical EWs in bright UV-selected galaxies at $z \sim 6$ (e.g. Curtis-Lake et al. 2012). VR7 consists of two resolved components in UV and [CII] emission (Matthee et al. 2019), similarly to other luminous galaxies at $z \approx 7$ (Ouchi et al. 2013; Sobral et al. 2015; Matthee et al. 2017b; Carniani et al. 2018b; Sobral et al. 2019). Do such multiple components influence measurements of velocity offsets with unresolved data (as e.g. Pentericci et al. 2016)? Is the Lyα emission around luminous LAEs at $z = 6.5$ more extended than typical LAEs at the same redshift, or more extended than galaxies at lower redshift? Can we witness any imprint of re-ionisation on the observed Lyα properties? These are the questions that we aim to address.

In this paper we focus on spatially resolved Lyα data from VLT/MUSE observations of the LAE 'VR7' (Matthee et al. 2017a) at $z = 6.532$. These data allow us to measure the Lyα extent and identify possible spatial variations in the Lyα line profile. An important aspect of this work is that we combine the resolved Lyα data with resolved [CII] spectroscopy from ALMA and resolved rest-frame UV imaging from *HST*/WFC3 (Matthee et al. 2019). This allows us to search for spatial variations in the velocity offset between Lyα and [CII] and to compare the extent of Lyα to the extent in the rest-frame UV.

The structure of this paper is as follows. We present the VLT/MUSE observations, data reduction and data quality

in §2. An overview of the known properties of VR7 is given in §3. We investigate the environment of VR7 in §4. In §5 we present the sizes and surface brightness profiles of VR7 in Lyα, [CII] and rest-frame UV and use the rest-frame UV data to separate Lyα emission that is extended beyond the rest-frame UV emission. We focus on resolving the Lyα line profile spatially in §6, where we also compare it to the resolved [CII] profile. Our results are placed in context in §7, where we discuss the Lyα extent and the Lyα velocity offset compared to other galaxies at $z \approx 3 - 7$. We summarise our results in §8. Throughout the paper we use a flat ΛCDM cosmology with $\Omega_M = 0.3$, $\Omega_\Lambda = 0.7$ and $H_0 = 70$ km s^{-1} Mpc^{-1}.

2 MUSE DATA

2.1 Observations & reduction

VR7 was observed with VLT/MUSE (Bacon et al. 2010) in service mode through program 099.A-0462 (PI: Matthee) on 29 May, 30 June, 28 July and 21 September 2017. Observations were performed with a seeing full-width half maximum (FWHM) $\approx 0.9 - 1.0''$ in the V-band and with an airmass ≈ 1.1. We used the standard Wide Field Mode with a field of view of $59.9'' \times 60.0''$ and pixel scale of $0.2''$/px, with a wavelength range 480-930 nm sampled by 3681 layers of $\Delta\lambda \approx 1.25$ Å. Individual exposure times were 720 s. We rotated the position angle by 90 degrees after each exposure and dithered by $2''$ in the RA/DEC direction with respect to the previous exposure. Two exposures were rotated by 120° and 240°. Combined, our exposures uniformly fill a grid of $70'' \times 60''$ centred on the position of VR7 with a maximum on target exposure time of 16740 s, or 4.65 hours.

We reduce the data using the MUSE pipeline v2.2 (Weilbacher et al. 2014) included in Esorex. We first run standard prescriptions for bias subtraction, flat-fielding, illumination correction and wavelength and flux calibration for each night individually. The coordinate system of each observation is mapped to the 2MASS (Skrutskie et al. 2006) reference frame in the same way as for our *HST* data and ground-based imaging (Matthee et al. 2015, 2019). Then, we use CubEx (Cantalupo in prep.; see Cantalupo et al. 2019 for a description) for additional flat-fielding, the additional removal of skyline residuals and the combination of the individual exposures. CubEx is run iteratively, where the white-light image (collapse of $\lambda = 4750 - 9350$ Å) of the first iteration has been used as a source mask for input in the final iteration. We manually add VR7 to the source mask, as it is un-detected in the white-light image due to its high redshift.

2.2 Quality and depth

We use a $I = 17$ magnitude star that is $9''$ away from the center of our pointing (see Fig. 1) to measure the point spread function (PSF) of our reduced MUSE data. At the wavelength of VR7's Lyα line, the PSF is well described by a Moffat profile with $\beta = 2.8$ (similar to Bacon et al. 2017) and FWHM=0.90$''$. The relative astrometric accuracy compared to the *HST*/WFC3 data (Matthee et al. 2019) is measured by comparing the positions of 44 objects detected in
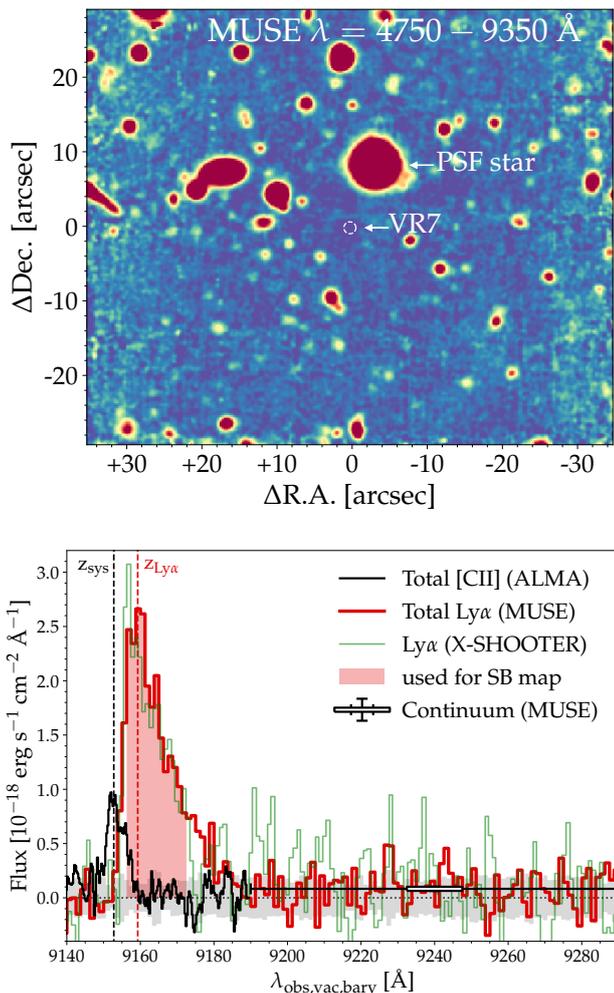
Figure 1. Top: White-light ($\lambda_{\rm obs,vac} = 4750 - 9350$ Å) image of the MUSE data, where the position of VR7 (not visible in the white-light image) and the star used for PSF-estimation are highlighted. Bottom: The 1D Lyα spectrum of VR7 as observed by MUSE in a 1.6″ diameter aperture (red), the X-SHOOTER Lyα spectrum (Matthee et al. 2017a; binned spectrally to match the MUSE resolution; green) and the total [CII] spectrum observed by ALMA (rescaling the observed frequency to the observed wavelength if [CII] were at $\lambda_0 = 1215.67$ Å; black). Lyα emission is detected over ≈ 22 Å, in 18 spectral layers and redshifted compared to [CII]. The red shaded area shows the wavelength range used to analyse the spatial distribution of Lyα emission ($\lambda_{\rm obs,vac} = 9153.5 - 9170$ Å; see §5.1). The grey shaded region shows the 1σ noise level derived by apertures in 62 empty sky positions. The white **rectangle** shows the flux density in the UV continuum measured by MUSE.

the white-light image of the MUSE data-cube. We find no significant offset with an accuracy of 0.02″.

We estimate the noise level of our data by measuring the standard deviation of the flux measured in 0.90″ diameter apertures in 62 empty-sky positions. These positions were carefully selected based on a PSF-matched χ^2-combined detection image based on ground-based *ugriz* and *HST* F110W and F160W data. The centres of the empty-sky positions are

> 2″ away from any detected object. The noise level depends on wavelength due to changes in the instrument efficiency, the sky brightness and atmospheric OH features, but it is relatively constant at rms=1×10^{-19} erg s^{-1} cm^{-2} Å^{-1} in individual layers around $\lambda_{\rm obs,air} \approx 915$ nm.

3 GENERAL PROPERTIES OF VR7

Here we present the global measurements of VR7 from the MUSE data, summarise the other multi-wavelength properties known about the galaxy and how they compare to the galaxy population at $z \sim 7$.

VR7's Lyα line is clearly detected in the MUSE data, with an integrated signal-to-noise S/N ≈ 40 in a narrow-band collapsed over $\lambda_{\rm obs,air} = 9153.5 - 9170.0$ Å ($\Delta v = 540$ km s^{-1}; found to optimise the S/N, see Fig. 1). The MUSE data also detects continuum right-wards of Lyα with an integrated S/N=3.8 from $920 - 930$ nm and an AB magnitude $25.16^{+0.40}_{-0.29}$, see Appendix A and the white symbol in Fig. 1. We fit the one-dimensional Lyα line profile with a skewed gaussian profile that is convolved with the line spread function (LSF) of the MUSE data (LSF-FWHM is **84** km s^{-1} at **the observed Lyα wavelength**; Bacon et al. 2017). Following e.g. Shibuya et al. (2014); Claeyssens et al. (2019), we parametrise the skewed gaussian profile as

$$f(\lambda) = A \exp\left(- \frac{\Delta v^2}{2(a_{\rm asym}(\Delta v) + d)^2} \right), \qquad (1)$$

where Δv **is the Lyα velocity with respect to the systemic redshift,** A is the normalisation, $a_{\rm asym}$ the asymmetry parameter and where d controls the line-width. By fitting to 1000 bootstrap-resamples of the data, we measure that Lyα flux peaks at $z = 6.534 \pm 0.001$, which corresponds to a velocity offset of $+213^{+19}_{-20}$ km s^{-1} to the systemic redshift traced by [CII]$_{158\mu m}$ ($z = 6.5285$; Matthee et al. 2019, see Fig. 1). The line-width FWHM is 374^{+21}_{-23} km s^{-1} and the best-fitted asymmetry $a_{\rm asym} = 0.34 \pm 0.03$. We measure an integrated Lyα luminosity of $(2.66 \pm 0.15) \times 10^{43}$ erg s^{-1}, which corresponds to an EW$_0 = 38 \pm 5$ Å when combined with the UV luminosity and slope (M$_{1500} = -22.37 \pm 0.05$, $\beta = -1.38^{+0.29}_{-0.27}$; Matthee et al. 2019). Our measurements from the MUSE, **HST and ALMA** data are summarised in Table 1. The Lyα luminosity is consistent with the slit-loss corrected flux (using the Lyα narrow-band) measured with X-SHOOTER (Matthee et al. 2017a).

Compared to the galaxy population at $z \sim 7$, VR7 has a high UV and Lyα luminosity (≈ 5 L$^\star_{\rm UV}$ and $2.5 \times$L$^\star_{\rm Ly\alpha}$, respectively). It is unclear whether the Lyα EW of VR7 is typical for its luminosity and redshift. Curtis-Lake et al. (2012) find that 50 % of >L$^\star_{\rm UV}$ galaxies at $z = 6.0 - 6.5$ have an EW$_0 > 25$ Å, while Furusawa et al. (2016) find no strong Lyα emission in nine observed LBGs at a photometric redshift $z \sim 7$. While the [CII]-UV luminosity ratio is representative of galaxies with similar luminosity (indicating a gas-phase metallicity ≈ 0.2 Z$_\odot$; Matthee et al. 2019), the upper limit on the IR-UV luminosity ratio (the latter constrained by $\lambda_0 = 160\mu m$ continuum observations) is extremely low, indicating faint IR luminosity and hence little obscured star formation yielding SFR$_{\rm UV+IR} = 54^{+5}_{-2}$ M$_\odot$ yr^{-1} (Matthee et al. 2019).

Table 1. Integrated measurements from the HST/WFC3, ALMA and MUSE data.

Property	Value
HST/WFC3 & ALMA	Matthee et al. (2019)
R.A.	22:18:56.36
Dec.	+00:08:07.32
M_{1500}	-22.37 ± 0.05
β	$-1.38^{+0.29}_{-0.27}$
$z_{\mathrm{sys,[CII]}}$	$6.5285^{+0.0007}_{-0.0004}$
$\mathrm{FWHM_{[CII]}}$	200^{+48}_{-32} km s^{-1}
$\mathrm{SFR_{UV+IR}}$	54^{+5}_{-2} M$_\odot$ yr^{-1}
MUSE	This paper
$z_{\mathrm{spec,Ly\alpha}}$	6.534 ± 0.001
$\Delta v_{\mathrm{Ly\alpha}}$	213^{+19}_{-20} km s^{-1}
$L_{\mathrm{Ly\alpha}}$	$(2.66 \pm 0.15) \times 10^{43}$ erg s^{-1}
$\mathrm{EW_{0,Ly\alpha}}$	38 ± 5 Å
$\mathrm{FWHM_{Ly\alpha}}$	374^{+21}_{-23} km s^{-1}
$a_{\mathrm{asym,Ly\alpha}}$	0.34 ± 0.03
$m_{\mathrm{AB,920-930nm}}$	$25.16^{+0.40}_{-0.29}$ (S/N=3.8)

Despite its luminosity, there are no clear indications of AGN activity in VR7. The Lyα EW$_0$ is easily explained by a star-forming nature. No strong rest-frame high-ionisation UV lines as NV, CIV or HeII are detected (Matthee et al. 2017a), the Lyα line is relatively narrow, significantly narrower than most (narrow-line) AGN (Sobral et al. 2018). Similar to other UV-luminous galaxies at $z \sim 7$ (e.g. Bowler et al. 2017) VR7's rest-frame UV emission is resolved into two components with effective radii $0.84 - 1.12$ kpc and comparable luminosity. This is further evidence against dominant single nuclear emission. We can not distinguish whether the UV and [CII] components in VR7 correspond to two individual galaxies that are merging, or two star-forming complexes within the same galaxy. The separations in terms of projected distance (~ 2kpc) and velocity (~ 200 km s^{-1}) are relatively small. The resolved [CII] spectroscopy does not reveal ordered rotation on these scales (Matthee et al. 2019), indicating that the two components do not belong to the same dynamical system. Individually, the components have UV sizes that are comparable to other galaxies. Therefore, we conclude that VR7 is a relatively typical luminous star-forming galaxy at $z \sim 6-7$ with the light being emitted roughly equally over two closely separated components.

4   ENVIRONMENT AROUND VR7

We use the MUSE data to search for LAEs in the vicinity of VR7 in order to assess whether it resides in an extreme overdense region. Specifically, we use CubEx to identify line-emitters in the continuum-subtracted data-cube observed at $\lambda_{\mathrm{air}} = 900 - 930$ nm. This wavelength range corresponds to $z = 6.403 - 6.651$, or $\Delta v = \pm 5000$ km s^{-1} with respect to VR7's systemic redshift. The area of our data is 1.076 arcmin^2, meaning that our comoving survey volume is 606.6 cMpc^3. In order to identify reliable emission-lines, we require that at least 30 connected voxels have an individual S/N of 1.8 (thus integrated S/N> 10).

Our search results in 18 emission lines, with fluxes in the range $(2.7 \pm 0.3) - (87.5 \pm 0.3) \times 10^{-18}$ erg s^{-1} cm^{-2}. We
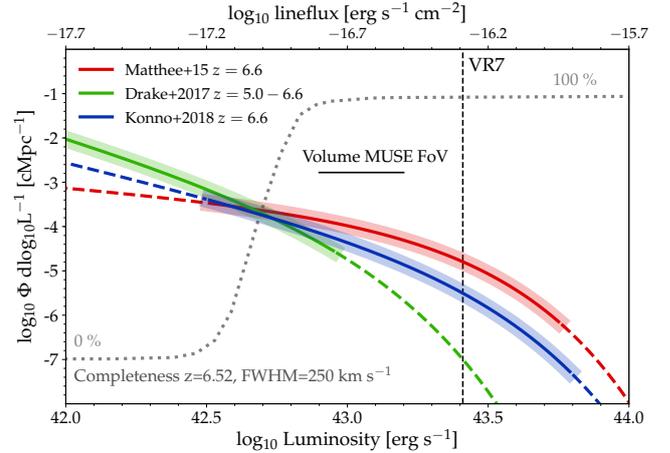

Figure 2. Lyα luminosity functions and completeness curve of our MUSE data. The blue and red LFs are from wide-field narrow-band surveys (Matthee et al. 2015; Konno et al. 2018) and the green LF is from a deep MUSE IFU survey (Drake et al. 2017). The line-style of the LFs changes to dashed in regimes where they are extrapolated, highlighting the complementarity of IFU and NB surveys. Shaded regions around the LFs highlight the uncertainties. The grey dotted line shows the completeness curve for simulated LAEs with line-width 250 km s^{-1} at $z = 6.52$. We also show the Lyα luminosity of VR7 and the volume probed at $z = 6.403 - 6.651$ in our MUSE data.

use the full wavelength range observed with MUSE to identify the redshift of each emission line. We detect two emission lines for three objects in the investigated wavelength range (either Hβ+[OIII]$_{4959}$ or [OIII]$_{4959}$+[OIII]$_{5007}$), meaning that 15 unique objects are found. A total of 10 objects are identified as [OIII] and/or Hβ emitters at $z = 0.82 - 0.92$, 3 objects are [OII] emitters at $z = 1.40 - 1.48$, 1 object is part of a [SII] doublet at $z = 0.34$ and 1 object is VR7 at $z = 6.53$. Therefore, no neighbouring LAEs are detected around VR7 above a S/N> 10.

The number of expected LAEs depends on the local (over)density and the luminosity function convolved with the completeness function of our data. We test the detection completeness of our data and methodology by injecting simulated LAEs in the data-cube and measuring the recovery fraction as a function of line-width and luminosity. We use IMFIT (Erwin 2015) to simulate the spatial profile of LAEs with the typical Lyα surface brightness profile of LAEs at $z = 5 - 6$ (Wisotzki et al. 2018), convolved with the PSF of our data. The Lyα flux is distributed over a half-gaussian line-profile (a gaussian with zero flux left-ward of the line-centre), which mimics the observed red asymmetric Lyα line profile of the majority of high-redshift LAEs. The line-profiles are smoothed with a gaussian line spread function with FWHM=85 km s^{-1} at the observed wavelength (Bacon et al. 2017). We inject 20 simulated LAEs at random positions in the data cube and store the recovered fraction after applying our source detection methodology. This process is repeated 50 times to increase the statistics. We vary the line-widths from 100-500 km s^{-1} in steps of 50 km s^{-1}, the total line-fluxes vary from 10^{-19} to 10^{-15} erg s^{-1} cm^{-2} and we vary the peak redshift from $z = 6.40 - 6.60$.
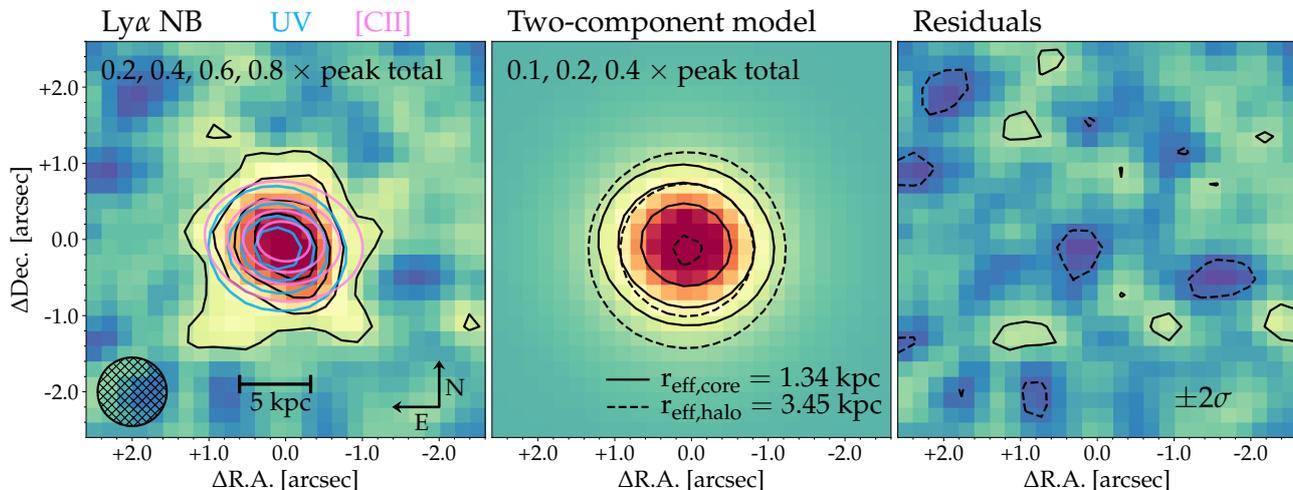
Figure 3. Continuum-subtracted Lyα image (left), best-fitted two-component model (middle) and the residuals (right). The Lyα image is constructed over $\lambda_{\rm obs,air} = 9153.5 - 9170.0$ Å in order to optimise the S/N, see Fig. 1 and §5.1. The outer 0.2× peak flux contours in the left panel correspond to the 3σ level. In the left panel, we also illustrate the rest-frame UV and [CII] morphology (from *HST*/WFC3 and ALMA; but convolved to the MUSE PSF as described in §5.2, see Matthee et al. 2019 for their images in higher resolution) in blue and pink, respectively. The black hashed circle shows the MUSE PSF-FWHM. The two-component model (§5.3) is a combination of an exponential UV-like core component (illustrated with solid contours; based on *HST* data) and a spherically symmetric exponential halo component (dashed contours).

The detection completeness depends strongly on the assumed line-width: i.e. a 50 % completeness (at $z = 6.52$, but with little dependence on redshift) is achieved at $L_{\rm Lya} = 2.8(4.2) \times 10^{42}$ erg s^{-1} for a line-width of 100 (200) km s^{-1}, while 50 % completeness is achieved only at $L_{\rm Lya} = 6.8 \times 10^{42}$ erg s^{-1} for lines with 400 km s^{-1}. Previous observations of LAEs at $z \sim 6.5$ show little dependence between line-width and luminosity (Matthee et al. 2017a), with a typical line-width 250 km s^{-1} (see also Herenz et al. 2019), which we use in our completeness estimate here.[1]

In Fig. 2 we show the Lyα luminosity function at $z = 6.6$ derived from narrow-band surveys from Matthee et al. (2015) and Konno et al. (2018), and the luminosity function at $z = 5.0 - 6.6$ from deep MUSE observations (Drake et al. 2017). Although the luminosity functions show some differences at the bright and faint end[2], their intersection point coincides with the luminosity at which our MUSE data is $\approx 50\%$ complete. As a consequence the predicted number of observed LAEs in the VR7 cube is not very sensitive to the differences in the luminosity functions, particularly since the VR7 cube probes a small cosmic volume. By integrating the luminosity functions convolved with the completeness curve, we find that 0.06-0.10 LAEs are expected to be identified between $z = 6.403 - 6.651$ in the VR7 cube

if it has a normal density. Since we do not identify a LAE besides VR7, we can thus exclude that the environment of VR7 is more than 10 times over-dense. Therefore, our MUSE data is not deep (and/or wide) enough to be used to identify moderate over-densities.

5 SIZES AND EXTENDED EMISSION

In this section, we investigate the extent of VR7's Lyα emission in the MUSE data and compare this to the rest-frame UV and [CII] sizes.

5.1 Lyα

We create a continuum-subtracted Lyα narrow-band image from the MUSE data-cube using a *HST*-based continuum model, convolved with the MUSE PSF with Imfit, see Appendix A for details. The continuum-subtracted Lyα image is shown in the left panel of Fig. 3. Due to the high *observed* Lyα EW ($\rm EW_{obs} = (1 + z)\, EW_0 = 286$ Å), the continuum subtraction does not impact the Lyα morphology significantly (the continuum contributes ≈ 8 % of the flux in the narrow-band over $\lambda = 9153.5 - 9170$ Å). We note that our continuum model is consistent with the continuum image from the MUSE data at 920-930 nm (Appendix A).

Lyα emission is well resolved in our MUSE data. We use Imfit to fit an exponential profile to VR7's Lyα image. In short, Imfit simulates PSF-convolved models (using the reference star image) and finds the best-fitting solution using the Levenberg-Marquardt algorithm. Uncertainties are estimated by performing the fitting procedure on 1000 bootstrap-resamples of the data using the propagated pixel-uncertainties and deriving 68.4 % confidence intervals.

---

[1] We retrieve similar results when using a (weakly) luminosity-dependent line-width following (Matthee et al. 2017a). The completeness function flattens in case line-widths follow a non-symmetric distribution (at fixed luminosity), but the shape and width of this distribution is currently not known and we therefore ignore scatter in line-widths at fixed luminosity.

[2] Note that the overlap in dynamic range between narrow-band surveys (which fixed the faint-end slope) and MUSE observations are limited.
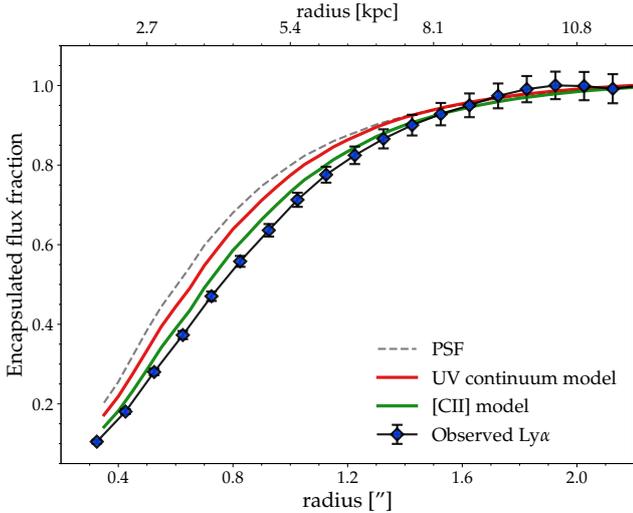
Figure 4. Curve-of-growth of VR7's Lyα emission (blue data-points), the *HST* based UV continuum model and ALMA based [CII] model convolved through the MUSE PSF (red and green lines, respectively) and the PSF in the MUSE data-set (grey dashed line). The Lyα emission, the [CII] emission and the UV continuum emission are extended, with Lyα having the largest scale length.

We do not impose spherical symmetry in these single component fits. We measure $r_{\rm eff,Ly\alpha} = 2.05 \pm 0.16$ kpc with $I_{\rm eff,Ly\alpha} = (3.39 \pm 0.45) \times 10^{-17}$ erg s^{-1} cm^{-2} arcsec^{-2}, the surface brightness at the effective radius. The best-fit ellipticity is $0.15^{+0.14}_{-0.06}$ with PA= 189^{+18}_{-33} degrees. If we allow the Sérsic index to vary between $n = 0.01$ and $n = 10$ we find a best-fit index $n = 0.55 \pm 0.42$ with a slightly larger scale radius, $r_{\rm eff,Ly\alpha} = 2.17 \pm 0.20$ kpc and similar ellipticity and position angle as the exponential model. Our results are listed in Table 2.

5.2 UV and [CII]$_{158\mu m}$

For a proper comparison to the rest-frame UV (*HST*/WFC3) and [CII] (ALMA) data, we use single exponential profiles to describe their morphologies using modelled images with the same PSF as the MUSE data. In their spatial resolution of $0.25''$ and $0.5''$, respectively, the morphology in both UV and [CII] is well described by a combination of two exponential components (Matthee et al. 2019) that are oriented in the east-west direction. However, most of this structure is not seen in the MUSE resolution due to the larger PSF (see the contours in the left panel of Fig. 3). Fitting the convolved UV and [CII] images with a single exponential profile as in §5.1, we measure (de-convolved) effective radii $r_{\rm eff,UV} = 1.34 \pm 0.06$ kpc and $r_{\rm eff,[CII]} = 2.14^{+0.24}_{-0.22}$ kpc (where the errors include propagating the uncertainties in the fits to the morphologies at higher resolution). The UV scale length is significantly smaller than the Lyα scale length (by a factor 1.5 ± 0.1), but the [CII] scale length is similar to Lyα, see Table 2. Note that we do not force spherical symmetry on our UV and [CII] models.

5.3 Two-component Lyα fit

The relatively large Lyα scale length compared to the UV continuum indicates the presence of a Lyα halo. Following the analyses by e.g. Steidel et al. (2011) and Wisotzki et al. (2016), we describe the Lyα surface brightness profile as the combination of a 'UV-like' component (the core-component; the MUSE-PSF-convolved *HST* model described above) that dominates in the centre and an exponential component that dominates at large radii (the halo-component). The centroids of the single-component Lyα models (§5.1) and the core-component are separated by only $0.04 \pm 0.01''$ (0.24 ± 0.09 kpc). Combined with the astrometric uncertainty of $0.02''$ this means there are no significant spatial offsets. Therefore, we assume the core and halo components to be co-spatial in our modelling below.

We use IMFIT to simulate a range of model images in a grid of halo flux, core flux and halo effective radius and then we calculate the χ^2 of each model compared to the continuum-subtracted Lyα image. For each model we also calculate the likelihood as $\mathcal{L} \propto \exp(-\chi^2/2)$. Each model consists of an exponential core component (with effective radius fixed to the UV size; $r_{\rm eff,core} = 1.34$ kpc, ellipticity 0.53 and position angle PA=74 degree) and a spherically symmetric halo component with effective radius $r_{\rm eff,halo} > 1.34$ kpc (Table 2). We find a best-fit halo effective radius $r_{\rm eff,halo} = 3.45^{+1.08}_{-0.87}$ kpc and a halo flux fraction of 54^{+11}_{-10} %. Here, the quoted values represent the median and the difference to the 16th and 84th percentile of the marginalised posterior distribution. Our results indicate that the majority of Lyα has a significantly different morphology from the UV. The best fit and its residuals are illustrated in Fig. 3.

5.3.1 1D SB profile

To facilitate comparison with literature results, we now focus on the (spherically averaged) 1D growth curve and surface brightness (SB) profile. We extract the 1D SB profile by measuring the summed flux in increasingly large concentric annuli, divided by the area of each annulus. Annuli are centred at the location of peak emission. The maximum annulus has a radius of $2''$. The errors on the 1D SB profile are estimated by extracting the SB profile in each of the 62 empty sky regions (see §2.2) and computing the standard deviation of the SBs in each annulus.

The observed growth curve of VR7's Lyα emission is shown in Fig. 4, where we also show the curves of the reference star used for the measurement of the PSF and of the (convolved) UV continuum and [CII] models. At the resolution of our MUSE observations VR7 is spatially resolved in UV, [CII] and Lyα emission, with increasing scale lengths, respectively. This is similar to the result by Fujimoto et al. (2019), who find a larger [CII] scale length than the UV scale length using stacks of galaxies at $z \sim 6 - 7$. In Fig. 5 we show how the 1D SB profile of VR7's Lyα emission is decomposed into the core and halo-components. These 1D SB profiles are measured on the best-fitted two-dimensional models described above. Halo flux overtakes that of the core Lyα flux at radii $> 0.8''$.
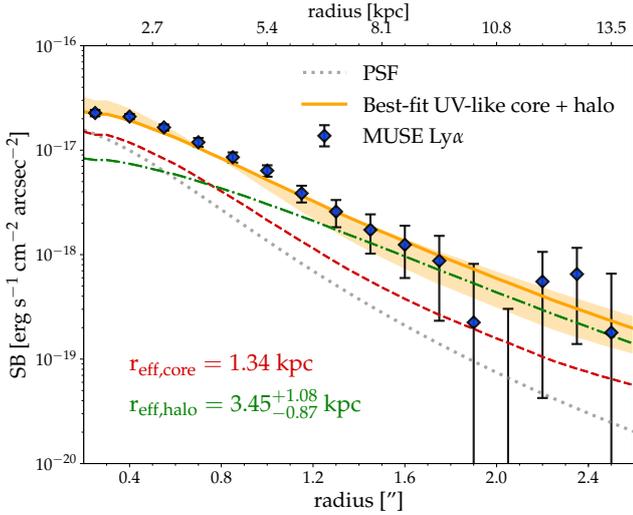
Figure 5. One-dimensional Lyα surface brightness profile of VR7 (blue points) and the best-fitted two component model and its uncertainties (orange line and shaded region). The dashed and dashed-dotted lines show the two components contributing to the Lyα SB profile, which consist of a core-like profile (red; with the same scale length as the UV continuum) and a halo-like profile (green; with larger scale length by definition), see §5.3. The grey dotted line shows the PSF. Note that while the shown SB profiles are the observed profiles (after PSF-convolution), our listed scale lengths are deconvolved values. With the current data, halo-like Lyα flux dominates at radii > 0.8″.

Table 2. Morphological measurements. The rest-frame UV measurement is performed on *HST* data that has been PSF-matched to the MUSE data.

Property	Value
MUSE Lyα	
Single component	
$r_{eff,Ly\alpha,exponential}$	2.05 ± 0.16 kpc
$ellipticity_{eff,Ly\alpha,exponential}$	$0.15^{+0.14}_{-0.06}$
$PA_{eff,Ly\alpha,exponential}$	189^{+18}_{-33}
$r_{eff,Ly\alpha,Sersic}$	2.17 ± 0.20 kpc
$ellipticity_{eff,Ly\alpha,Sersic}$	$0.17^{+0.11}_{-0.05}$
$PA_{eff,Ly\alpha,Sersic}$	189^{+17}_{-25}
n_{Sersic}	0.55 ± 0.42
UV-like core + spherical Lyα halo	
$r_{eff,Ly\alpha,halo}$	$3.45^{+1.08}_{-0.87}$ kpc
UV	
$r_{eff,UV,core}$	1.34 ± 0.06 kpc
$ellipticity_{UV}$	0.53 ± 0.05
PA_{UV}	74 ± 4
[CII]	
$r_{eff,[CII]}$	$2.14^{+0.24}_{-0.22}$ kpc
$ellipticity_{[CII]}$	0.76 ± 0.12
$PA_{[CII]}$	80 ± 6

6 RESOLVED LYα PROPERTIES

At the spatial resolution of the ALMA and *HST*/WFC3 data, VR7 is observed to consist of multiple components, while at the MUSE resolution the Lyα emission appears to be described by a single component in a standard collapsed pseudo-NB image. By exploiting the full 3D information of the MUSE data, together with higher spatial resolution ALMA and *HST* data, we explore whether multiple components can also be related to the Lyα emission, particularly in the line of sight.

6.1 Lyα line-profile variations

Here we investigate spatial variations in the Lyα line-profile and how these variations correlate with spatial variations in the [CII] emission line profile (Fig. 15 in Matthee et al. 2019). We explore spatial variations in the Lyα line profile by using position-velocity diagrams (PV diagrams; i.e. pseudo-slits) extracted over different regions of the galaxy. The benefit of PV diagrams is that they increase the S/N (by averaging over multiple pixels) without parametrising the data.

Fig. 6 shows PV diagrams in two halves of VR7. The extractions are centred on the peak Lyα emission and averaged over a 1.0″ slice in the orthogonal direction. As a reference velocity, we use the flux-weighted [CII] redshift, $z = 6.5285$ (Matthee et al. 2019), which we refer to as the 'systemic' redshift below. The left panel in Fig. 6 shows variations in the east-west direction, while the right panel shows variations in the north-south direction. The central row shows the PV diagrams, while the top and bottom rows show the 1D spectra by summing the PV diagrams ±1″ from the centre.

Two distinct spatial variations in the Lyα line profile can be identified in Fig. 6, which interestingly can also be identified in the [CII] spectra from ALMA (here imaged with spatial resolution with PSF-FWHM ≈ 0.7″; Matthee et al. 2019). In general, Lyα is redshifted by ≈ 220 km s^{-1} compared to the [CII] line. In the east however, we observe a second bump in the Lyα emission line at ≈ +600 km s^{-1} with respect to the systemic redshift, while the Lyα line in the west is broader. The Lyα line FWHM in the east is 230^{+80}_{-40} km s^{-1}, while it is 360^{+20}_{-40} km s^{-1} in the west. The second bump in the east is also seen in [CII] emission at a redshift of ≈ +130 km s^{-1} compared to the systemic. In [CII] emission, the second bump has a smaller velocity difference to the main component than the second Lyα bump has compared to the Lyα peak. There is a small tentative gradient in the peak-velocity of both the [CII] and Lyα lines. The peak shifts by ≈ +40 km s^{-1} from east to west and from north to south (see Fig. 14 in Matthee et al. 2019 for a [CII] moment map that shows this more clearly).

6.2 Lyα shell models

In order to interpret the spatial variations in the Lyα profile using Lyα information alone, we perform 'shell-model' fitting on continuum-subtracted Lyα spectra in different regions (the four directions in the PV-diagram; Fig. 6) of VR7 using the pipeline described in Gronke et al. (2015). The shell-model is a popular model in order to extract physical information of Lyα spectra. It consist out of a Lyα and continuum emitting source which is surrounded by a shell
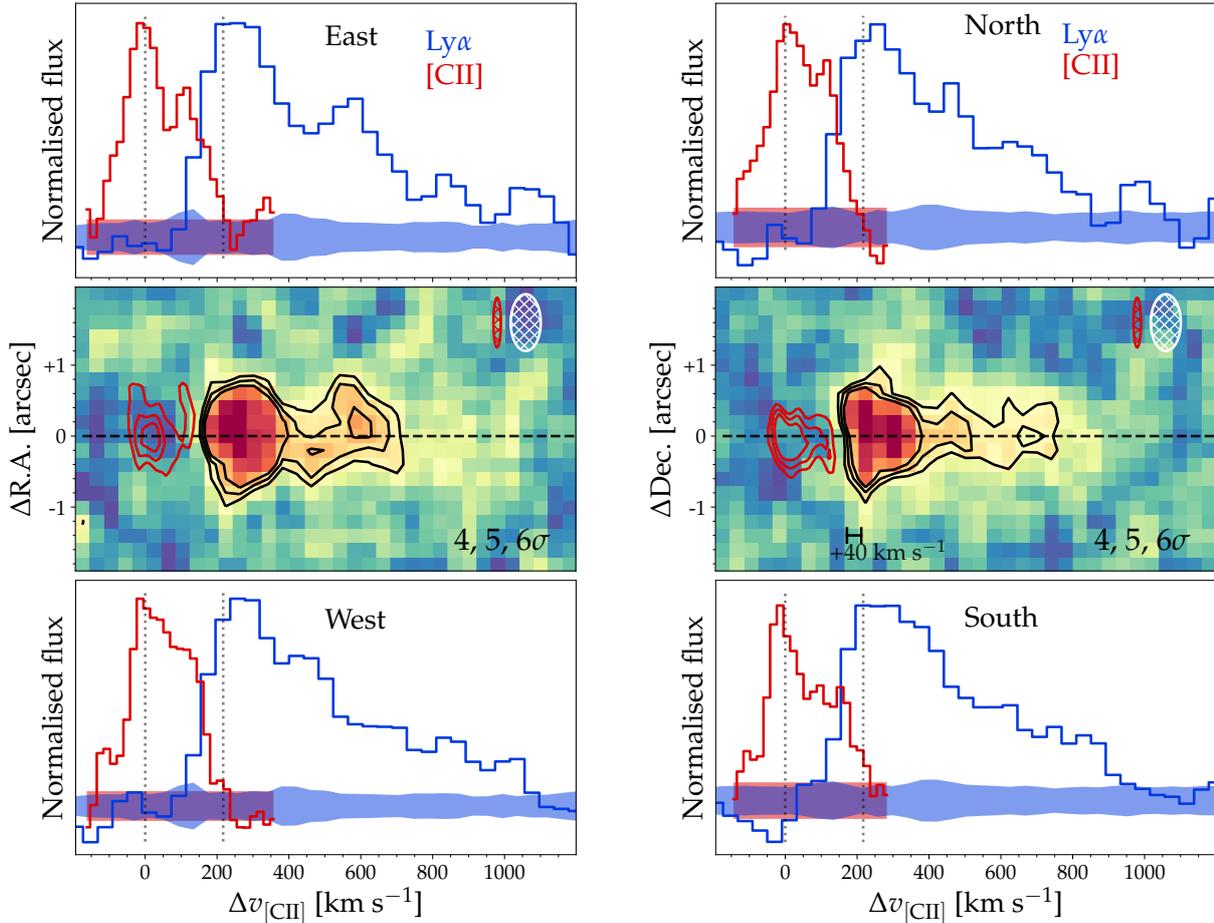
Figure 6. Spectral variations of [CII] and Lyα for VR7, depending on R.A. (left) and Dec. (right). Top and bottom rows show 1D extractions in Lyα (blue, extracted from the centre to ±1″) and [CII] (red, from ALMA; Matthee et al. 2019). The middle row shows the Lyα pseudo-slit, where black (red) contours mark the 4, 5, 6σ levels of the MUSE (ALMA) data. The white (red) ellipses show the PSF and LSF of the MUSE (ALMA) data. A second Lyα component is clearly visible towards the east, while the western component is broader. The peak of the Lyα line in the south/west is tentatively shifted by ≈ 40 km s^{-1} compared to the north/east.

of neutral hydrogen, and dust (Ahn et al. 2002; Verhamme et al. 2006). The model features a minimum of six free parameters: the width and equivalent width of the intrinsic Lyα line (σ_i, EW_i), the dust and hydrogen content of the source (which we characterize by the all-absorbing dust optical depth τ_a, and the neutral hydrogen column density of the shell $N_{\rm HI}$), the 'effective temperature' of the shell T, and the inflow / outflow velocity of the shell $v_{\rm exp}$. The Bayesian fitting pipeline used features the possibility to add additional parameters. We also leave the systemic redshift as an additional free parameter on which we impose the gaussian prior $(\mu, \sigma) = (6.5285, 0.001)$ based on [CII]. We note that leaving $z_{\rm sys}$ free to vary is important as even a small shift can cause a sharp drop in likelihood. We also note that the LSF is incorporated in the fitting pipeline by smoothing the synthetic spectrum before computing the likelihood.

We show the best fitted models in Fig. 7 (as black, solid lines in each panel). The shell model can describe the data in various positions of the galaxy very well. The systemic redshift obtained from the fit is consistent with the prior [CII] spectrum, but it is at slightly higher redshift than the [CII] peak (by +70 km s^{-1}). This could be due

to the fact that VR7 is a two-component galaxy, see §6.3. The intrinsic spectrum of the shell model fits is in all cases somewhat broader than the [CII] spectrum. By analysing the shell-model spectra, we found that the secondary red peak (particularly prominent in the east) consists mainly of so-called 'backscattered' photons, which are photons with a last scattering angle $\cos\theta \sim -1$. These photons experience a boost of ~ 2 times the shell outflow velocity, thus leaving a characteristic 'hump' in the emergent Lyα spectrum (Ahn et al. 2002). The best-fit shell model parameters vary from $N_{\rm HI} \sim 10^{20}$cm^{-2} in the east to $N_{\rm HI} \sim 10^{20.4}$ cm^{-2} in the west, and the outflow velocities from 320 km s^{-1} to 360 km s^{-1}, respectively. These parameters are larger than those found in the luminous LAE CR7 (Dijkstra et al. 2016). We note that the physical nature of the shell-model parameters is still debated (e.g. Orlitová et al. 2018). One caution is that Lyα photons trace preferably the low-$N_{\rm HI}$ medium, and thus, the spectral information does not necessarily correspond to the line-of-sight physical conditions (Eide et al. 2018; Kakiichi & Gronke 2019). We interpret these results in §7.4.
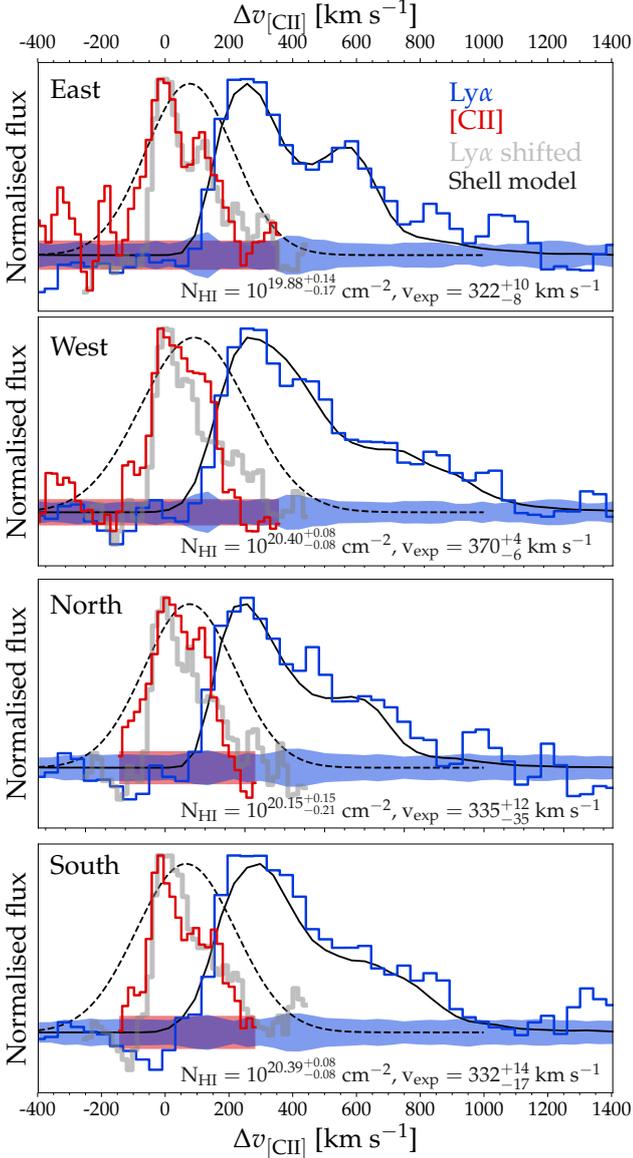
Figure 7. 1D extractions of the spectral variations of [CII] (red) and Lyα (blue) for VR7, depending on position (as Fig. 6). The solid black lines show the best-fitted Lyα shell models and the dashed black lines show the intrinsic spectrum in those models. The intrinsic spectrum in the shell model fits is somewhat broader and redshifted compared to [CII]. We show in light-grey an artificial Lyα profile shifted as $v_{new} = (v_{obs} - 260 \text{ km s}^{-1})/2.6$ km s^{-1} (**see §7.4**). It is remarkable that it resembles the [CII] profile in the east so well, but this could be a coincidence.

6.3 Two Lyα emitting components?

One explanation of the resemblance between the spatial variations in the [CII] and Lyα line profiles could be that the Lyα emission in VR7 also consists of components in the line of sight with slight velocity differences, each emitting Lyα.

In order to optimally isolate the two components identified in the PV diagram spatially, we collapse the MUSE data-cube over customized wavelength layers. Specifically, we collapse the layers from $v = 220 - 340$ km s^{-1} (where $v = 0$ is the systemic redshift $z = 6.5285$) to isolate the

main peak and $v = 540 - 580$ km s^{-1} to isolate the redshifted bump, see Fig. 8. While the large PSF significantly challenges the analysis, it is clear that the emission in the redshifted bump extends more towards the east, while the main component extends towards the south-west. Fitting the light-distribution with a single exponential similar to §5.1, we find that the peak position of the redshifted bump is shifted by $0.14 \pm 0.04''$ towards the east compared to the main component. Note however that the red asymmetric wing of the main component likely contributes to the image of the bump emission, indicating the real separation can be higher. The redder Lyα component is tentatively more extended (with an effective radius of 2.71 ± 0.35 kpc compared to 2.14 ± 0.26 kpc).

For comparison, in Fig. 8, we also show the (MUSE PSF-convolved) contours of the individual components identified in the rest-frame UV. Similarly to Lyα, the components are mostly separated in the east-west direction and the western component extends somewhat towards the south. In case we interpret that the Lyα emission is indeed the combination of two LAEs for which we see the systemic redshifts in [CII] emission, we infer that the main component has a Lyα peak separation $\Delta v_{Ly\alpha} = +213^{+19}_{-20}$ km s^{-1} and that the redder component has $\Delta v_{Ly\alpha} = +457^{+24}_{-19}$ km s^{-1}. This indicates that the two components have different HI column densities (e.g. Verhamme et al. 2006). We discuss this interpretation in §7.4.

7 DISCUSSION

The re-ionisation of the Universe is likely still ongoing at $z \approx 6.5$, with a global neutral fraction of ≈ 40 % (e.g. Naidu et al. 2019). This could significantly impact the local UV background and therefore the HI structures in the nearby CGM of galaxies (e.g. Mas-Ribas et al. 2017; Sadoun et al. 2017), particularly for star-forming galaxies that are still in a local neutral bubble. Naively, one would expect that galaxies that reside in such a significantly more neutral environment have flatter Lyα SB profiles and observed Lyα lines with higher velocity shift (due to an increased importance of resonant scattering and the IGM damping wing), compared to post-re-ionisation LAEs (e.g. Dijkstra et al. 2007). Are the Lyα properties of VR7 different from similar and lower-redshift galaxies? We now compare the observed spatial and spectral Lyα properties of VR7 to comparable galaxies at $z = 5 - 6$ (i.e. just after re-ionisation) and other galaxies at similar redshift.

7.1 Is Lyα emission more extended at $z > 6$ than at later times?

In Fig. 9, we compare the UV continuum and Lyα halo scale lengths of VR7 to measurements of individual LAEs at $z = 5 - 6$ by Leclercq et al. (2017) and stacked LAEs at $z = 5.7 - 6.6$ by Momose et al. (2014). We also compare the continuum scale length to a stack of UV-selected galaxies at $z = 5 - 7$ by Fujimoto et al. (2019). We note that we use our measurements based on a single UV component in VR7 to resemble the techniques in other works.

As seen in Fig. 9, the rest-frame UV continuum scale length is observed to increase with luminosity and VR7 and
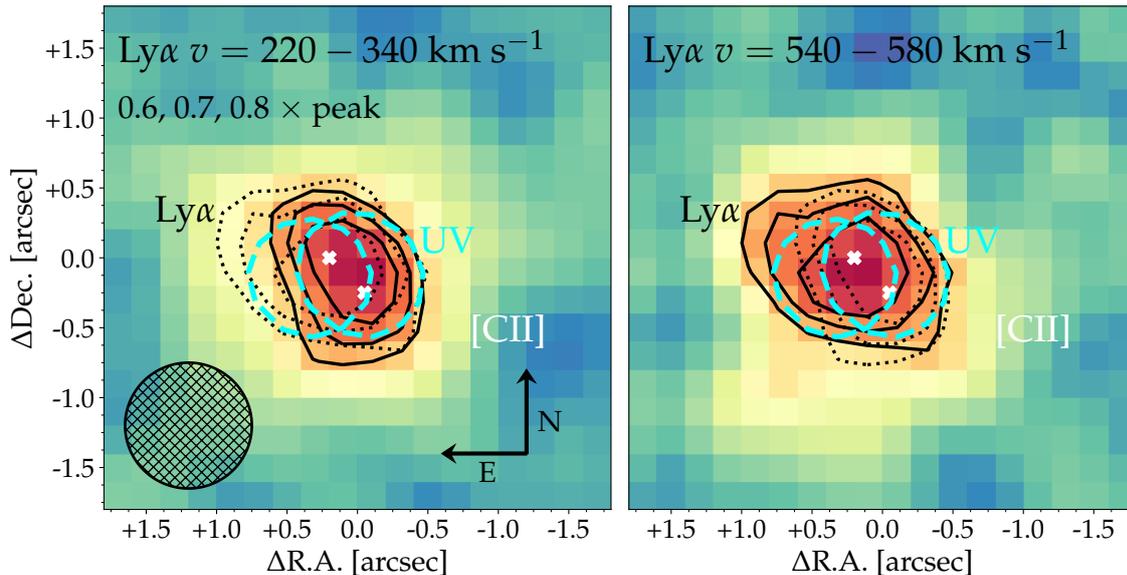
Figure 8. Lyα narrow-band images centred on the main peak (left) and on the "bump" (right) identified in the PV diagrams (Fig. 6). Solid black contours mark the 0.6, 0.7 and 0.8 × the peak flux in each collapsed image, while the dotted black contours illustrate the contour levels from the other component, respectively. The black hashed circle shows the PSF of the MUSE data. The dashed cyan contours show the 0.6× peak UV flux in MUSE-PSF convolved model images of the individual components. White crosses mark the peak positions of the [CII] components.

its individual components follow this trend, with no indications of evolution with redshift. The Lyα halo scale length does not show a clear dependence on luminosity or redshift. While Momose et al. (2014) find a larger scale length at $z = 6.6$ compared to $z = 5.7$, the measured scale length at $z = 6.6$ is similar to some individual LAEs at $z < 6$ observed by Leclercq et al. (2017). The halo scale length of VR7 is very comparable to the most luminous system in the sample from Leclercq et al. (2017), but smaller than the scale length of typical LAEs at $z \approx 6.5$. These results highlight that there is significant variation in halo scale lengths at fixed redshift and UV luminosity. There are no significant differences between the Lyα halo scale-lengths of VR7 and galaxies at $z < 6$, which is expected if the HI column densities in the CGM are comparable (e.g. Sadoun et al. 2017). Larger samples with better overlapping dynamic ranges are required both at $z > 6$ and $z = 5 - 6$ in order to identify more subtle, potentially luminosity dependent trends.

7.2 Is there evolution of Lyα velocity offsets at $z > 6$?

Lyα observables are affected by gas on the interstellar medium (ISM), CGM, and IGM scales. Understanding the interplay of these scales is important, especially at higher redshifts where Lyα is used to put constraints on the epoch of reionisation. For example, the observed velocity offset between Lyα and the systemic redshift is an important ingredient in using the Lyα-emitting fraction of high-redshift galaxies to measure the neutral fraction of the IGM (e.g. Mason et al. 2018). However, if there are smaller velocity offsets at $z \approx 7$ compared to $z \approx 5$ due to an evolution in the ISM or CGM, the fraction of galaxies observable in Lyα emission will be lower at $z \approx 7$ compare to $z \approx 5$ (e.g. Choudhury

et al. 2014), even though there could be no difference in IGM properties.

Therefore, evolution in the intrinsic velocity offset is degenerate to an evolution of the neutral fraction in the IGM, which also decreases the observed fraction of Lyα emitters (e.g. Pentericci et al. 2016). Additionally, it has been argued (e.g. Stark et al. 2017; Mason et al. 2018) that, due to outflows, the Lyα velocity offset is larger in more luminous systems, facilitating their Lyα observability in the epoch of reionisation. However, the interpretation of large *observed* velocity offsets may be challenging in the epoch of re-ionisation. The IGM damping wing could cut-off a significant fraction of the flux on the blue parts of the line if a galaxy is surrounded by significant amounts of hydrogen (e.g. Miralda-Escudé & Rees 1998; Dijkstra et al. 2007; Laursen et al. 2011; Smith et al. 2019). This will result in a large observed velocity offset. This could well be the case in the galaxy B14-65666 at $z \approx 7$ which has a Lyα velocity offset of $\approx +800$ km s^{-1} (Hashimoto et al. 2018) and an accordingly low Lyα EW.

As the number of Lyα resonant scattering events is highly sensitive to the HI column density (Neufeld 1991), a smaller Lyα velocity shift is found in case the ISM is more ionised (Barnes et al. 2011) or more porous (e.g. Gronke & Dijkstra 2016; Smith et al. 2019). Early results from ALMA measurements of the $[OIII]_{88\mu m}/[CII]_{158\mu m}$ ratio in a few galaxies indeed indicate a highly ionised ISM in galaxies at $z \sim 7$ (Inoue et al. 2016; Carniani et al. 2017; Hashimoto et al. 2018). In Fig. 10 we compare the velocity shift between the observed peak of the Lyα emission to the systemic redshift ($\Delta v_{Ly\alpha}$) with the width of nebular, non-resonant emission lines. We compare VR7 to other UV and Lyα selected galaxies at $z \sim 6 - 7$ (for which [CII] is used as nebular line) and to LAEs at $z = 2 - 3$ (for which $[OIII]_{5007}$ is used; Erb

et al. 2014). VR7 has rather typical line-width and velocity shift for the $z \approx 6 - 7$ population, although there may be significant dispersion for individual components. **Both** the mean **and median** observed velocity shifts in galaxies at $z \sim 6 - 7$ are smaller than in Lyα emitters at $z \sim 2 - 3$ at fixed nebular line-width, particularly at $\sigma \approx 200$ km s^{-1}, although we note there is large scatter. This similarly points towards a more ionised ISM in observed LAEs at $z \sim 6 - 7$.[3]

The implication of lower observed velocity shifts at high-redshift is that the majority of galaxies at $z \sim 6 - 7$ that are observed in Lyα emission do not experience a strong additional HI damping wing compared to galaxies at $z \sim 2 - 3$. In combination with the Lyα surface brightness profile this suggests that there is no detectable neutral hydrogen enhancement in both down-the-barrel and transverse direction. This agrees with the scenario that these galaxies reside in relatively large ionised regions.

7.3 How well can [CII] be used to measure Lyα velocity offsets?

One potential caveat for using [CII] as a proxy to obtain the true systemic redshift is that [CII] has a lower ionisation energy than hydrogen. Because of this, the observed [CII] emission can trace a variety of gas phases. In local low-metallicity star-forming galaxies [CII] is predominantly comes from neutral gas (Cormier et al. 2019), but [CII] may also originate from HII regions or trace molecular gas (Zanella et al. 2018). If there are velocity differences between the regions which emit [CII] and the region that emit Lyα (i.e. HII regions), [CII] would not be an accurate means of systemic redshift. Furthermore, [CII] emission could trace neutral gas on which Lyα photons resonantly scatter. On the other hand, observations of both [CII] and [OIII] lines in galaxies at $z \sim 7$ find consistent redshifts and line-widths (Hashimoto et al. 2018; Walter et al. 2018), suggesting that there is no problem in using [CII] for measuring Lyα velocity offsets. Moreover, observations of [CII] and molecular lines in sub-millimetre galaxies at $z \sim 5$ also report consistent systemic redshifts (e.g. Riechers et al. 2014; Jiménez-Andrade et al. 2018).

Another caveat in interpreting Lyα velocity shifts is whether Lyα spectra are observed at the same spatial locations as [CII]. In VR7, we identify a (slight) spatial gradient in the peak velocities of both lines (§6.1). Typically Lyα spectra of galaxies in the epoch of re-ionisation are obtained through narrow slits and can thus suffer from such intrinsic line profile variations. In VR7, [CII] is more extended than the UV continuum emission and resembles the Lyα extent. Interestingly, in the luminous LAE 'Himiko' at $z = 6.59$, the Lyα peak SB coincides with the peak in [CII] SB (and not with one of the UV components; Carniani et al. 2018a). Furthermore, the [CII] emission that coincides with the region where Lyα peaks is emitted at a different velocity from the regions where [CII] and the rest-frame UV overlap. However, such offsets between Lyα and the UV are not seen in other luminous LAEs like CR7 (e.g. Sobral et al. 2019) and VR7 (e.g. Matthee et al. 2017b, 2019). Future joint spatially

resolved, high resolution spectroscopy of Hα and Lyα emission would relieve these caveats, but current instruments can already be used to explore whether important spatial variations and offsets between Lyα, UV and [CII] are also present in other galaxies.

7.4 On the origin of variations in the the Lyα profile in VR7

In §6 we showed that the Lyα profile in VR7 has significant spatial variations. Do these variations originate in the emitting gas distribution and kinematics (for example two merging galaxies) or are they mostly driven by differences in the scattering medium, or both?

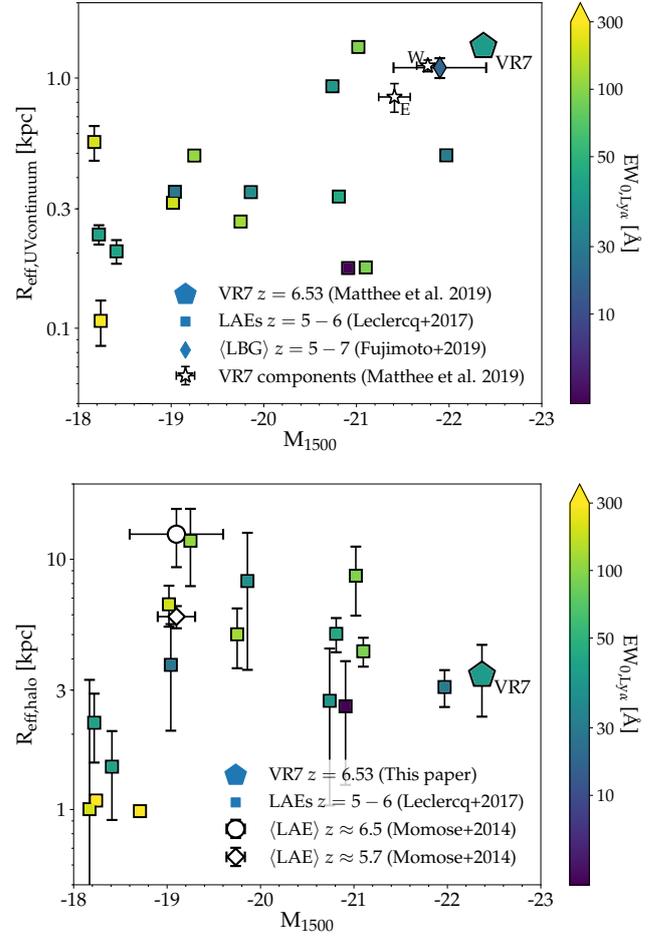The fact that the positions of the Lyα components

---

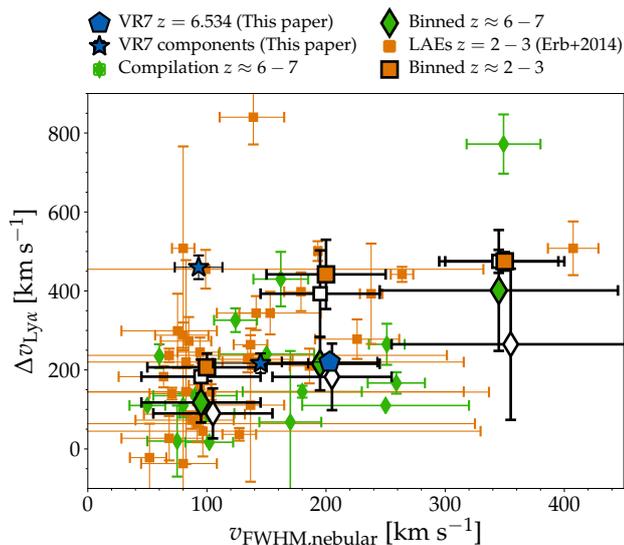
Figure 9. The dependence of UV (top panel) and Lyα (bottom panel) scale-length on the UV continuum luminosity for VR7 and a comparison sample of LAEs at $z = 5 - 6$ from Leclercq et al. (2017). We computed the median UV luminosity of the sample from Momose et al. (2014) using measurements of the same galaxy sample from Ono et al. (2010). We also show the two individual UV components of VR7 as measured in Matthee et al. (2019). The continuum scale length increases with luminosity and VR7 follows the trend of galaxies at $z = 5 - 6$. There is no clear dependence between Lyα halo scale length and luminosity and VR7 has similar Lyα halo scale length as galaxies at LAEs $z = 5 - 6$.

Figure 10. The velocity offset between Lyα and the systemic redshift, $\Delta v_{\mathrm{Ly}\alpha}$, versus the nebular line-width (traced by [CII] or [OIII]). We show measurements for VR7 (total as blue pentagon; individual components as blue stars), a compilation of galaxies at $z \approx 6-7$ (green diamonds) and Lyα emitters at $z \approx 2-3$ from Erb et al. (2014) (orange squares). Larger symbols show *mean* velocity offsets in bins of line-width, where the error bars show the error on the mean. *Median* velocity offsets are shown with larger white-filled symbols. Galaxies at high-redshift have lower *observed* velocity offsets than galaxies at $z \approx 2-3$. This indicates that the ISM in galaxies at $z \approx 6-7$ is more ionised and that there is little additional absorption from circum/inter-galactic gas compared to galaxies at lower redshift.

(main peak and 'bump') differ and resemble the positions of the UV and [CII] components (Fig. 8) indicates towards a scenario where the variations are mainly driven by the emitting gas distribution. The dynamical information of the components seen in [CII] emission is not fully lost in the observed Lyα line profile, indicating the Lyα line profile is determined to large extent by processes relatively close to the galaxy.

The grey lines in Fig. 7 show the Lyα profile where the velocity axis is shifted as $v_{\mathrm{new}} = (v_{\mathrm{obs}} - 260 \ \mathrm{km \ s^{-1}})/2.6$ km s^{-1}. The values of 260 km s^{-1} and 2.6 are motivated as they best match the peak separation in the [CII] line. It is surprising that this simple re-scaled version of the Lyα profile is able to resemble the red part of the [CII] profile well, particularly in the east. This requires a relatively specific distribution of expansion velocities and hydrogen column densities, in particular to have similar relative fluxes of the peaks. Within our limited current knowledge of the ISM properties of VR7, variations in the HI column densities and kinematics are plausible. The eastern part of the galaxy has a lower [CII]-UV ratio compared to the western part (Matthee et al. 2019), which could indicate low gas density (Ferrara et al. 2019). Future resolved multiple-line characterisation of the ISM properties in VR7 are required to address this question in more detail.

8 CONCLUSIONS

In this paper, we have presented spatially resolved Lyα spectroscopy of VR7 (Matthee et al. 2017a) with VLT/MUSE. VR7 is a luminous star-forming galaxy at $z = 6.53$ that is resolved in two components in the UV and [CII]. Lyα emission is detected with an integrated S/N≈ 40 and well resolved spatially and spectrally. We showed that the MUSE data is not deep and/or wide enough to accurately quantify the over-density of LAEs around VR7, only ruling out over-densities of a factor > 10. We connected the Lyα line profile of VR7 to the velocity properties of the ISM (as traced by the [CII] emission observed by ALMA) for the first time at the epoch of re-ionisation. We searched for specific imprints of incomplete re-ionisation on the observed Lyα properties of VR7, such as a strongly broadened and/or redshifted and/or largely extended Lyα line, but find no significant trend. Our main results are the following:

- Lyα emission (with a line-width FWHM=374^{+21}_{-23}km s^{-1}) in VR7 is more extended than the UV continuum, with a scale length $r_{\mathrm{eff,Ly}\alpha} = 2.05 \pm 0.16$ kpc compared to $r_{\mathrm{eff,UV}} = 1.34 \pm 0.06$ kpc (§5.1). The scale length of [CII] emission is similar to Lyα with $r_{\mathrm{eff,[CII]}} = 2.14^{+0.24}_{-0.22}$ kpc (§5.2). Combining the Lyα with the UV data, we de-convolve the Lyα emission in a UV-like component and an extended halo-component with scale length $r_{\mathrm{eff,Ly}\alpha,\mathrm{halo}} = 3.45^{+1.08}_{-0.87}$ kpc (§5.3). The halo scale length is comparable to UV-bright LAEs at $z = 5-6$ observed by MUSE, but smaller (by a factor ≈ 3.5) than the stacked halo scale length of fainter LAEs at $z = 6.6$ (Fig. 9).

- We identify spatial variations in the Lyα line profile (§6.1). There is a tentative weak gradient in the peak velocity, redshifted by ≈ 40 km s^{-1} in the south-western side of the galaxy compared to the north-east. We identify a redshifted bump in the eastern part of the Lyα line, which is redshifted by ≈ 230 km s^{-1} with respect to the main Lyα peak (Fig. 6). According to the shell-model, the bump could correspond to back-scattering photons, but we find that the relative positions of the main Lyα component and the bump resemble those of components identified in *HST* rest-frame UV data. These components have a projected separation of ≈ 2kpc (Fig. 8).

- The main peak of the Lyα line is offset by $+213^{+19}_{-20}$ km s^{-1} compared to the main peak of the [CII] line, but the spatial variations seen in the Lyα profile qualitatively resemble the variations in the [CII] line (Fig. 6). [CII] displays a similar, weak, peak gradient and a second eastern component. However, the [CII] line-width is narrower than Lyα and the velocity separation between the [CII] peak and the [CII] bump is smaller (by a factor ≈ 2). While a single shell model can accurately fit the Lyα profiles in different locations in the galaxy, its fitted intrinsic lines are somewhat redshifted and broader compared to the observed [CII] widths (Fig. 7). The spatial and spectral resemblance of [CII] and Lyα indicates that the total observed Lyα emission in VR7 likely originates from (at least) two spatially and spectrally distinct regions. As the velocity offsets between the Lyα line and [CII] vary between the components, different HI column densities are plausibly present.

- Using a literature compilation, we find that the velocity offsets between Lyα and the systemic are smaller at $z \approx 6-7$ than found in LAEs at $z \approx 2-3$ at fixed nebular line-width

(Fig. 10). This indicates that the ISM in observed higher redshift galaxies is more ionised than at $z \approx 2 - 3$. The observed Lyα photons from galaxies at $z \approx 6 - 7$ do not experience a strong additional HI damping wing compared to galaxies at $z \sim 2 - 3$. Therefore, these galaxies (including VR7) likely reside in relatively large ionised bubbles.

Our work reveals that constraints on the epoch of reionisation relying on Lyα observables need to take the potential evolution in the neutral hydrogen properties of the ISM and CGM into account. This will likely loosen the existing constraints significantly. The solution to break the major degeneracies is to explore the evolution of other Lyα observables such as the SB profile and the spectral properties as well as their correlation with different measurements. In this work we show the potential of such efforts on an individual galaxy. This can be put on solid, statistical grounds with larger future programs.

REFERENCES

Ahn S.-H., Lee H.-W., Lee H. M., 2002, ApJ, 567, 922
Astropy Collaboration et al., 2013, AAP, 558, A33
Bañados E., et al., 2018, Nature, 553, 473
Bacon R., et al., 2010, in Ground-based and Airborne Instrumentation for Astronomy III. p. 773508, doi:10.1117/12.856027
Bacon R., et al., 2017, AAP, 608, A1
Barnes L. A., Haehnelt M. G., Tescari E., Viel M., 2011, MNRAS, 416, 1723

Bertin E., 2006, in Gabriel C., Arviset C., Ponz D., Enrique S., eds, Astronomical Society of the Pacific Conference Series Vol. 351, Astronomical Data Analysis Software and Systems XV. p. 112
Bertin E., 2010, SWarp: Resampling and Co-adding FITS Images Together, Astrophysics Source Code Library (ascl:1010.068)
Bertin E., Arnouts S., 1996, AAPS, 117, 393
Bowler R. A. A., et al., 2017, MNRAS, 466, 3612
Cantalupo S., et al., 2019, MNRAS, 483, 5188
Carniani S., et al., 2017, AAP, 605, A42
Carniani S., et al., 2018a, MNRAS, 478, 1170
Carniani S., Maiolino R., Smit R., Amorín R., 2018b, ApJL, 854, L7
Choudhury T. R., Puchwein E., Haehnelt M. G., Bolton J. S., 2014, arXiv:1412.4790,
Claeyssens A., et al., 2019, MNRAS, 489, 5022
Cormier D., et al., 2019, arXiv e-prints, p. arXiv:1904.08434
Curtis-Lake E., et al., 2012, MNRAS, 422, 1425
Dijkstra M., 2014, PASA, 31, 40
Dijkstra M., Lidz A., Wyithe J. S. B., 2007, MNRAS, 377, 1175
Dijkstra M., Gronke M., Sobral D., 2016, ApJ, 823, 74
Drake A. B., et al., 2017, AAP, 608, A6
Eide M. B., Gronke M., Dijkstra M., Hayes M., 2018, ApJ, 856, 156
Erb D. K., et al., 2014, ApJ, 795, 33
Erwin P., 2015, ApJ, 799, 226
Fan X., et al., 2006, AJ, 132, 117
Ferrara A., Vallini L., Pallottini A., Gallerani S., Carniani S., Kohandel M., Decataldo D., Behrens C., 2019, arXiv e-prints, p. arXiv:1908.07536
Fujimoto S., Ouchi M., Ferrara A., Pallottini A., Ivison R. J., Behrens C., Gallerani S., 2019, arXiv e-prints,
Furusawa H., et al., 2016, ApJ, 822, 46
Gronke M., Dijkstra M., 2016, ApJ, 826, 14
Gronke M., Dijkstra M., Trenti M., Wyithe S., 2015, arXiv:1502.00022,
Hashimoto T., et al., 2018, arXiv e-prints,
Herenz E. C., et al., 2019, AAP, 621, A107
Hu E. M., Cowie L. L., Barger A. J., Capak P., Kakazu Y., Trouille L., 2010, ApJ, 725, 394
Hunter J. D., 2007, Computing in Science and Engineering, 9, 90
Inoue A. K., et al., 2016, Science, 352, 1559
Jiménez-Andrade E. F., et al., 2018, AAP, 615, A25
Jones E., Oliphant T., Peterson P., et al., 2001–, SciPy: Open source scientific tools for Python, http://www.scipy.org/
Kakiichi K., Gronke M., 2019, arXiv e-prints,
Kakuma R., et al., 2019, arXiv e-prints, p. arXiv:1906.00173
Konno A., et al., 2018, PASJ, 70, S16
Laursen P., Sommer-Larsen J., Razoumov A. O., 2011, ApJ, 728, 52
Leclercq F., et al., 2017, AAP, 608, A8
Mas-Ribas L., Hennawi J. F., Dijkstra M., Davies F. B., Stern J., Rix H.-W., 2017, ApJ, 846, 11
Mason C. A., et al., 2018, ApJL, 857, L11
Matthee J., Sobral D., Santos S., Röttgering H., Darvish B., Mobasher B., 2015, MNRAS, 451, 400
Matthee J., Sobral D., Darvish B., Santos S., Mobasher B., Paulino-Afonso A., Röttgering H., Alegre L., 2017a, MNRAS, 472, 772
Matthee J., et al., 2017b, ApJ, 851, 145
Matthee J., et al., 2019, arXiv e-prints,
Miralda-Escudé J., Rees M. J., 1998, ApJ, 497, 21
Momose R., et al., 2014, MNRAS, 442, 110
Naidu R. P., Tacchella S., Mason C. A., Bose S., Oesch P. A., Conroy C., 2019, arXiv e-prints,
Neufeld D. A., 1991, ApJL, 370, L85
Ono Y., Ouchi M., Shimasaku K., Dunlop J., Farrah D., McLure R., Okamura S., 2010, ApJ, 724, 1524

Orlitová I., Verhamme A., Henry A., Scarlata C., Jaskot A., Oey M. S., Schaerer D., 2018, AAP, 616, A60

Ouchi M., et al., 2013, ApJ, 778, 102

Pentericci L., et al., 2014, ApJ, 793, 113

Pentericci L., et al., 2016, ApJL, 829, L11

Planck Collaboration et al., 2015, arXiv:1502.01582,

Riechers D. A., et al., 2014, ApJ, 796, 84

Rivera-Thorsen T. E., et al., 2015, ApJ, 805, 14

Sadoun R., Zheng Z., Miralda-Escudé J., 2017, ApJ, 839, 44

Santos S., Sobral D., Matthee J., 2016, MNRAS, 463, 1678

Shibuya T., et al., 2014, ApJ, 785, 64

Skrutskie M. F., et al., 2006, AJ, 131, 1163

Smith A., Ma X., Bromm V., Finkelstein S. L., Hopkins P. F., Faucher-Giguère C.-A., Kereš D., 2019, MNRAS, 484, 39

Sobral D., Matthee J., Darvish B., Schaerer D., Mobasher B., Röttgering H. J. A., Santos S., Hemmati S., 2015, ApJ, 808, 139

Sobral D., et al., 2018, MNRAS, 477, 2817

Sobral D., et al., 2019, mnras, 482, 2422

Stark D. P., Ellis R. S., Chiu K., Ouchi M., Bunker A., 2010, MNRAS, 408, 1628

Stark D. P., et al., 2017, MNRAS, 464, 469

Steidel C. C., Bogosavljević M., Shapley A. E., Kollmeier J. A., Reddy N. A., Erb D. K., Pettini M., 2011, ApJ, 736, 160

Taylor M., 2013, Starlink User Note, 253

Verhamme A., Schaerer D., Maselli A., 2006, AAP, 460, 397

Walter F., et al., 2018, ApJL, 869, L22

Weilbacher P. M., et al., 2014, in Manset N., Forshay P., eds, Astronomical Society of the Pacific Conference Series Vol. 485, Astronomical Data Analysis Software and Systems XXIII. p. 451 (arXiv:1507.00034)

Wisotzki L., et al., 2016, AAP, 587, A98

Wisotzki L., et al., 2018, Nature, 562, 229

Zanella A., et al., 2018, MNRAS, 481, 1976

van der Walt S., Colbert S. C., Varoquaux G., 2011, Computing in Science and Engineering, 13, 22

APPENDIX A: CONSISTENCY CHECK HST BASED CONTINUUM - MUSE CONTINUUM

In the main text we subtract the UV continuum flux in the Lyα narrow-band using a model based on *HST*/WFC3 data. In this model, VR7 is described by a combination of two exponential profiles separated by $0.35''$ with scale lengths of 0.84 and 1.12 kpc and contributing 36 and 64 % to the total flux, respectively (see Matthee et al. 2019 for details). We use IMFIT (Erwin 2015) to create a model image that is convolved with the MUSE-PSF and normalise the flux based on extrapolating the UV luminosity and slope at $\lambda_0 = 1500$ Å to the $\lambda_0 \approx 1230$ Å. Once the model is convolved with the MUSE-PSF, it is well-fitted by a single exponential profile with $r_{eff} = 1.34$ kpc (after again accounting for the PSF).

We perform a consistency check by comparing the UV continuum at $\lambda_0 \approx 1230$ Å in our MUSE data to the prediction based on our model. The result is shown in Fig. A1. The left panel shows the detection of the UV continuum in our MUSE data (with S/N$\approx$ 4), while the middle panel shows the convolved *HST* based model. The right panel shows that no significant residuals are seen (except for the amplification of a negative noise peak already present in the data), providing a rough validation of our model.

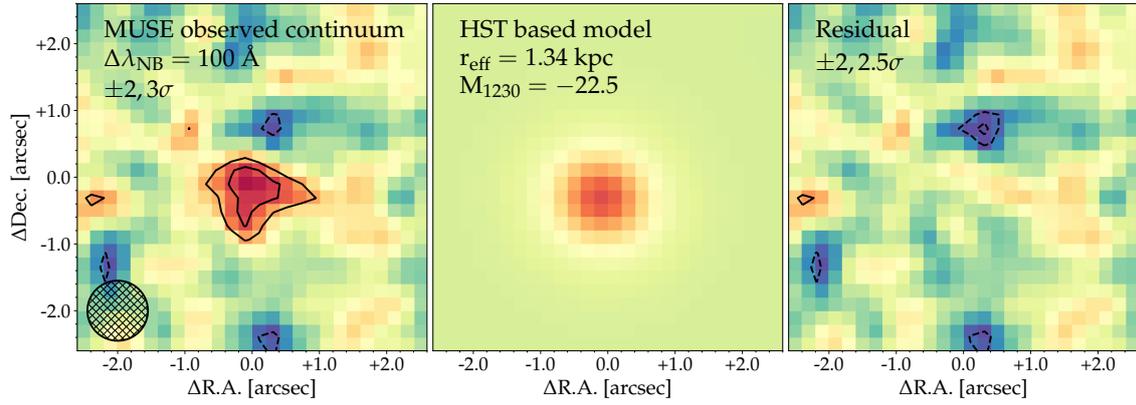This paper has been typeset from a TeX/LaTeX file prepared by the author.

Figure A1. Validation of our continuum subtraction model. The left panel shows the continuum detected in a collapsed image of $\lambda_{obs} = 920 - 930$ nm in the MUSE cube. The middle panel shows the UV continuum model based on convolving the *HST* morphology with the MUSE PSF. The right panel shows the residual image.